Journal of Cleaner Production 544 (2026) 147676

Contents lists available at ScienceDirect

Journal of Cleaner Production

journal homepage: www.elsevier.com/locate/jclepro

Effect of palladium loading on catalytic performance and product selectivity during diclofenac degradation by Pd^0@anaerobic activated sludge

Xiaodi Li [a,b], Jingzhou Zhou [a,b], Lin Yang [c], Si Pang [c], Yi Yang [a,b], Defu Gan [d], Junxia He [a,b], Penghui Shi [b,e], Siqing Xia [a,b,*]

[a] State Key Laboratory of Pollution Control and Resource Reuse, College of Environmental Science and Engineering, Tongji University, Shanghai, 200092, China
[b] Shanghai Institute of Pollution Control and Ecological Security, Shanghai, 200092, China
[c] Eco-environmental Protection Research Institute, Shanghai Academy of Agricultural Sciences, Shanghai, 201403, China
[d] Key Laboratory of Jiangxi Province for Functional Biology and Pollution Control in Red Soil Regions, School of Life Sciences, Jinggangshan University, Ji'an, 343009, China
[e] Shanghai University of Electric Power, Shanghai, 200090, China

HIGHLIGHTS

- Pd^0@AAS catalyze sequential hydrodechlorination and aromatic ring hydrogenation for DCF.
- Low Pd loading favors cost-effective dechlorination alone for DCF.
- Total hydrogenation is essential to eliminate chronic toxicity for DCF.
- Hydrogenation demands higher Pd loading for contiguous active sites.
- Guides the design of cost-effective Pd catalysts for DCF detoxification.

GRAPHICAL ABSTRACT

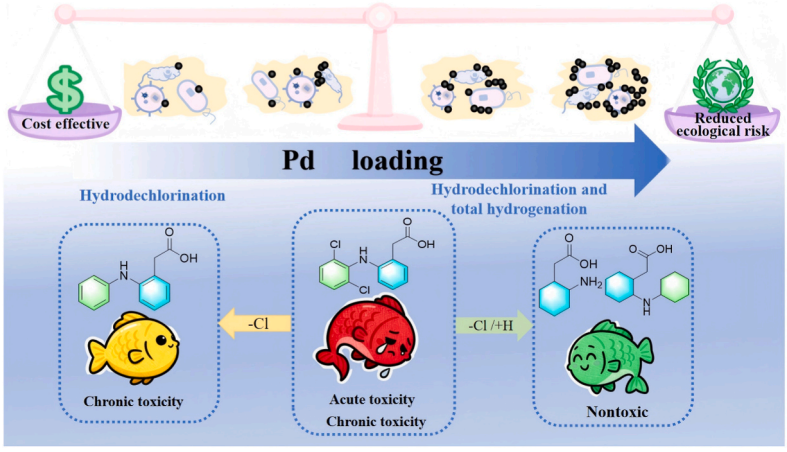

ARTICLE INFO

Keywords:
Catalytic hydrodechlorination
Aromatic hydrogenation
Pharmaceutical degradation
Ecotoxicity assessment
Halogenated aromatic pollutants

ABSTRACT

Anaerobic activated sludge (AAS) was used to fabricate a biomass-supported palladium nanocatalyst (Pd^0@AAS) with varied Pd loading via a green biosynthesis route that eliminates the need for toxic reagents and high energy input. This catalyst was subsequently evaluated for the catalytic degradation of diclofenac (DCF). The degradation pathway was systematically elucidated, focusing on the influence of Pd loading on product selectivity, reaction kinetics, and corresponding ecotoxicological outcomes. Pd^0@AAS detoxified DCF via two key steps: hydrodechlorination of DCF to 2-anilinophenylacetic acid (APA), followed by aromatic ring hydrogenation of

* Corresponding author. College of Environmental Science and Engineering Tongji University, 1239 Siping Road, Shanghai, 200092, China.
E-mail addresses: siqingxia@gmail.com, siqingxia@tongji.edu.cn (S. Xia).

https://doi.org/10.1016/j.jclepro.2026.147676
Received 15 October 2025; Received in revised form 14 January 2026; Accepted 25 January 2026
Available online 30 January 2026

APA. After 4 h, low Pd loading (1.1 wt%) resulted in high selectivity toward APA (89.7 %), whereas high Pd loading (10.6 wt%) promoted complete hydrogenation, reducing APA selectivity to 0 %. Ecotoxicity estimates indicated that hydrodechlorination effectively eliminated acute toxicity, whereas full hydrogenation was required to eliminate chronic toxicity. Kinetic analysis showed that the hydrodechlorination rate constant increased with Pd loading (1.1–10.6 wt%), yet catalyst-specific activity (normalized to Pd concentration) reached a plateau at Pd loading 5.3 wt%, beyond which nanoparticle aggregation limited further enhancement—indicating that higher Pd loadings are economically impractical for dechlorination alone. In contrast, both the reaction rate constant and catalyst-specific activity of hydrogenation increased strongly across the same Pd loading range. The values at 10.6 wt% were 2.7-fold and 30-fold higher than those at 5.3 wt% and 2.7 wt%, respectively. This difference underscores a greater reliance on contiguous Pd^0 active sites for hydrogenation of aromatic rings. These findings guide the optimization of biomass-supported Pd^0 nanocatalysts for cost-effective and ecologically safe remediation of halogenated aromatic pollutants.

1. Introduction

Diclofenac (DCF) is a priority pollutant due to its environmental persistence and ecotoxicity. Approximately 75 % of consumed DCF enters ecosystems via incomplete wastewater treatment (Schmidt et al., 2018), with conventional plants removing only 21–40 % (Zhang et al., 2008), leading to its widespread detection in aquatic environments (Dalahmeh et al., 2020; Qiu et al., 2024). DCF contamination poses severe ecological threats, including catastrophic vulture declines (Oaks et al., 2004), bioaccumulation in consumable produce (Bartrons and Peñuelas, 2017; González García et al., 2018), and stimulation of microcystin production (Kwidzińska et al., 2024). Its high mobility via microplastics (Xu et al., 2025) and toxicity at trace concentrations (Fontes et al., 2018) amplifies concerns about DCF. Current DCF removal techniques have major limitations. Adsorption merely transfers the contaminant, while microbial degradation is kinetically slow (Chhaya et al., 2025; Li et al., 2022). Although advanced oxidation processes achieve high removal efficiency (Sales et al., 2025), they often generate toxic by-products and involve high operational costs (Zhao et al., 2022). Therefore, developing integrated strategies that combine efficient degradation with minimal ecological risk is imperative (Nosek and Zhao, 2024).

Precious metal-based nanocatalysis (particularly elemental palladium (Pd^0) nanoparticles) has emerged as a sustainable remediation strategy. Pd^0 nanoparticles enable efficient hydrodehalogenation of DCF under ambient conditions, utilizing molecular hydrogen (H_2) as a clean electron donor (De Corte et al., 2012). The reaction mechanism involves the generation of highly reductive atomic hydrogen (H*) at the Pd^0 surface, which exhibits exceptional reactivity in substituting chlorine atoms within halogenated organic compounds. Conventional chemical synthesis of Pd^0 nanoparticles, while enabling control over size and morphology, often involves toxic chemicals, generates secondary toxic waste, and incurs high costs. In contrast, microbial synthesis provides an eco-friendly and cost-effective alternative, minimizing the use of toxic agents (Law et al., 2022). The use of biomass as a support further adds to the advantages of such systems. Furthermore, biomass-supported Pd^0 nanocatalysts demonstrate enhanced resistance to chloride and sulfide-induced deactivation compared to free nanoparticles (Quan et al., 2019). This is possibly due to the adsorption of chloride and sulfide species by microbes and extracellular polymeric substances (EPS). Additionally, Pd integrated with biomass enables the simultaneous reduction of DCF and other oxidizing pollutants like nitrate. Anaerobic activated sludge (AAS), readily available from wastewater treatment plants, represents a particularly versatile biomass support. It inherently possesses pollutant treatment capabilities and serves as an in-situ reductant, capping agent, and carrier for synthesizing Pd^0 nanoparticles (Zhou et al., 2020), facilitating the preparation of Pd^0@AAS. The application of this biosynthesized Pd^0@AAS composite for catalytic DCF degradation represents an eco-friendly strategy that synergistically integrates biological synthesis with catalytic degradation processes.

Pd^0 nanoparticles mediate two critical detoxification pathways: Hydrodehalogenation: substitution of halogen atoms (Cl in DCF) with hydrogen, reducing lipid solubility and bioaccumulation potential (He et al., 2021). Hydrogenation: hydrogenation of aromatic rings or carbon-carbon double bonds to form saturated structures, enhancing biodegradability and reducing toxicity. For instance, Pd^0 nanoparticles demonstrate dual catalytic functionality in hydrodehalogenation and total hydrogenation processes: (1) Complete hydrodechlorination of trichloroethylene (TCE) coupled with hydrogenation yields ethane as the terminal product (De Corte et al., 2011), and (2) Stepwise transformation of 4-chlorophenol (4-CP) occurs through initial hydrodechlorination to phenol, which is subsequently hydrogenated to cyclohexanone and cyclohexanol (Baeza et al., 2016; Long et al., 2021). Notably, the aryl halide hydrodehalogenation predominantly occurs under moderate conditions (ambient temperature, neutral pH). However, the subsequent hydrogenation of the resulting aromatic intermediates can present a greater energetic challenge, particularly for structurally complex molecules like DCF (Nieto-Sandoval et al., 2018). This contrasts with other halogenated aromatics such as tetrabromobisphenol A (TBBPA) where hydrogenation under milder conditions may be more facile (Nieto-Sandoval et al., 2022). While hydrodehalogenation reduces acute toxicity, residual aromatic structures in dehalogenated products may retain ecological risks due to their recalcitrance to microbial degradation.

Therefore, achieving controllable selectivity between dechlorination and hydrogenation pathways represents a key challenge and opportunity in designing catalysts for the targeted degradation of DCF. Several studies have demonstrated the efficacy of Pd^0-catalyzed dechlorination of DCF, exemplified by Quan et al.'s pioneering work utilizing anaerobic granular sludge-synthesized Pd^0 nanoparticles for efficient hydrodechlorination (Quan et al., 2019). However, these studies have predominantly focused on dechlorination efficiency while neglecting subsequent hydrogenation. Given that Pd loading critically influences both catalytic efficiency and product selectivity (Luo et al., 2022), this study systematically investigates: degradation pathways of DCF via AAS-synthesized Pd^0 nanoparticles under H_2 electron donation; Pd loading-dependent modulation of hydrodechlorination vs. hydrogenation efficiencies; environmental implications of transformation product profiles.

2. Methods and materials

2.1. Chemicals and materials

Disodium tetrachloropalladate (Na_2PdCl_4, ≥98 % purity, precursor for the preparation of Pd^0) and DCF (≥99 % purity) were procured from Macklin Biochemical Co., Ltd. (Shanghai, China). The molecular structure and electrostatic potential mapping of DCF are provided in Fig. S1. High-purity hydrogen (H_2, 99.999 %) and nitrogen (N_2, 99.999 %) gases were obtained from Wendong Chemical Co., Ltd (Shanghai, China). The AAS used to produce Pd^0 nanoparticles was initially sourced from the secondary sedimentation tank in the Bailonggang wastewater treatment plant (Shanghai, China) and then acclimated with nitrate to establish a

stable and efficient denitrifying capacity. This enhanced reductive capability is pivotal for the subsequent effective reduction of Pd^{2+} ions to form Pd^0 nanoparticles. All other reagents were analytical grade unless stated otherwise.

2.2. Preparation and characterization of Pd^0 nanoparticles on anaerobic activated sludge (Pd^0@AAS)

The Pd^0 nanocatalyst was biosynthesized and supported on anaerobic activated sludge (AAS), with the resulting material denoted as Pd^0@AAS, via a routine procedure under anaerobic conditions with H_2 as the electron donor (**Text S1** for full details). The AAS biomass content was kept constant across all experiments. Catalysts with Pd loadings of 1.1, 2.7, 5.3, and 10.6 wt% were synthesized by varying the initial Na_2PdCl_4 concentration, while maintaining a constant AAS biomass concentration of 2 g of volatile suspended solid per liter (VSS/L). The detailed composition of the anaerobic mineral medium used for catalyst synthesis is summarized in Table S1.

The Pd concentration was determined by inductively coupled plasma optical emission spectrometry (ICP-OES). The crystal structure, surface elemental composition, and morphology of the catalyst were characterized by X-ray diffraction (XRD), X-ray photoelectron spectroscopy (XPS), and transmission electron microscopy with energy-dispersive X-ray spectroscopy (TEM-EDS), respectively. The size distribution of Pd nanoparticles was determined by measuring 150 particles from random TEM fields of view using Image J software. The corresponding nanoparticle size data are provided in Table S2. Detailed specifications of the instruments and the corresponding operational parameters are provided in **Text S2**.

2.3. Catalytic activity of the Pd^0@AAS towards DCF

The catalytic activity of the Pd^0@AAS in DCF degradation was evaluated through batch experiments conducted in crimp-sealed anaerobic vials (total volume: 125 mL; working volume: 50 mL). The experimental protocol involved the sequential additions of Pd^0@AAS catalysts, phosphate-buffered saline (PBS, pH 7.4 ± 0.2), and DCF into the reaction system. The catalysts with Pd loadings of 1.1, 2.7, 5.3, and 10.6 wt% were each dosed to achieve a consistent AAS concentration of 2 g VSS/L. Consequently, the total amount of active Pd^0 particles was not held constant but increased with the nominal Pd loading. The observed trends in activity and selectivity are therefore discussed in the context of varying Pd quantity. The final concentration of DCF was maintained between 90 and 120 μM in all experiments. After that, the vials were flushed with N_2 for 5 min to remove dissolved O_2, then tightly sealed with stoppers, evacuated, and subsequently filled with 75 mL H_2 (approximately 3.0 mmol at 30 °C and 1 atm). This amount of H_2 was in substantial excess (>60-fold) of the stoichiometric requirement for the complete hydrogenation of all DCF present in the system. To ensure adequate adsorption of DCF onto the catalyst prior to the catalytic reaction, the introduction of H_2 was deliberately initiated after a pre-contact time of >40 min (Barreto Torres et al., 2022) between Pd^0@AAS and DCF. Reactions were initiated by incubating the vials on a temperature-controlled orbital shaker (30 °C ± 0.5 °C, 180 rpm). At predetermined intervals, samples (1 mL) were aseptically withdrawn via gas-tight syringes and immediately filtered through 0.45 μm polyethersulfone (PES) membranes (Titan Scientific, 25 mm diameter) to terminate catalytic activity.

2.4. Analysis methods

Intermediate products were identified by ultra-high-performance liquid chromatography-mass spectrometry (UPLC-MS), and DCF and its products were quantified using high-performance liquid chromatography (HPLC). Definitive structural confirmation by nuclear magnetic resonance (NMR) spectroscopy was not performed, as direct analysis within the complex anaerobic sludge matrix was prevented by overwhelming background interference from the biomass, which would mask the signals of the target intermediates. Cl^- concentration was determined using an ion chromatograph (Aquion, Thermo Fisher, USA) equipped with an AS-19 column and a suppressed conductivity detector. Detailed instrument specifications and operational parameters are provided in **Text S3**. Detailed analytical procedures and parameters are summarized in Table S3.

2.5. Calculations

The product selectivity for an intermediate can be calculated by Eq. (1):

$$[S_x]_t = \frac{[C_x]_t}{[C_{DCF}]_0 - [C_{DCF}]_t} \quad (1)$$

where $[S_x]_t$ and $[C_x]_t$ represent the proportion of product x at reaction time t and its concentration in the liquid phase, respectively. $[C_{DCF}]_0$ and $[C_{DCF}]_t$ represent the initial concentration and the concentration at reaction time t of DCF, respectively.

Based on experience observations and theoretical deduction, the process of Pd^0@AAS catalyzed hydrodechlorination of DCF and hydrogenation of 2-anilinophenylacetic acid (APA) can be described using a pseudo-first-order kinetic model (Nieto-Sandoval et al., 2018):

$$-\frac{dC_{DCF}}{dt} = k_1 C_{DCF} \quad (2)$$

$$-\frac{dC_{APA}}{dt} = k_2 C_{APA} - k_3 C_{DCF} - k_4 C_{Cl-APA} \quad (3)$$

Where C_{DCF}, C_{APA} and $C_{Cl\text{-}APA}$ (μM) are the aqueous phase concentration of DCF, APA and 2-(2-((2-chlorophenyl)amino)phenyl)acetic acid (Cl-APA). And k_1 (min^{-1}) is the apparent rate constant of DCF hydrodechlorination, k_2 (min^{-1}) is the apparent rate constant of APA hydrogenation, k_3 (min^{-1}) and k_4 (min^{-1}) represent the apparent rate constants for the generation of APA by DCF and Cl-APA, respectively. When both DCF and Cl-APA in the system are depleted, the kinetic model of hydrogenation of APA can be simplified as follows:

$$-\frac{dC_{APA}}{dt} = k_2 C_{APA} \quad (4)$$

The normalized values of hydrodechlorination and hydrogenation first-order rate constants to Pd (i.e., catalytic-specific activities) k_{Pd1}, k_{Pd2} ($L{\cdot}mmol^{-1}$-Pd$\cdot$ min^{-1}) were calculated from:

$$k_{Pd1} = \frac{k_1}{C_{Pd}} \quad (5)$$

$$k_{Pd2} = \frac{k_2}{C_{Pd}} \quad (6)$$

where C_{Pd} (mM) is the Pd concentration.

3. Results and discussion

3.1. Characterization of Pd^0 nanoparticles in AAS

Fig. 1(a) depicts the XRD pattern of Pd within the AAS matrix, revealing characteristic metallic diffraction features. Prominent diffraction peaks observed at $2\theta = 40.1°$, $46.7°$, and $68.1°$ are indexed precisely to the (111), (200), and (220) crystallographic planes, respectively, of the face-centered cubic (fcc) Pd (JCPDS No.46-1043). This confirms that Pd in the AAS samples assumes a crystalline form, with the (111) plane (octahedral morphology) (Ding et al., 2018) being the most prevalent facet. The diffraction data demonstrate the successful incorporation and crystallization of Pd within the AAS matrix.

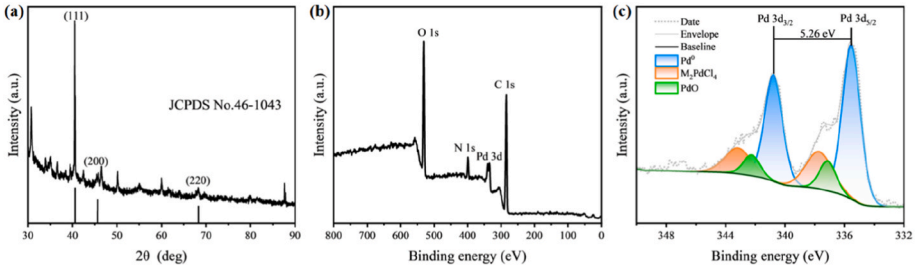

Fig. 1. XRD pattern (a), survey XPS spectrum (b) and high-resolution Pd 3d XPS spectrum (c) acquired from Pd in AAS (Pd loading 2.3 wt%).

Fig. 1(b) displays the XPS survey spectrum of Pd^0@AAS, which confirms the coexistence of characteristic elements C, N, O (originating from AAS) and metallic Pd species in the catalyst system. To gain deeper insights into the surface chemistry of Pd nanoparticles within the AAS, high-resolution Pd 3d XPS measurements were carried out. The resultant XPS spectrum, as depicted in Fig. 1(c), exhibits well-defined peaks at 335.54 eV and 340.78 eV, which unequivocally correspond to the characteristic Pd 3d doublet for metallic palladium (Pd^0). The XPS analysis, however, identifies a small amount of unreduced $PdCl_4^{2-}$ complexes (14.85 %) and PdO species (7.35 %) in the catalyst matrix. The oxidized Pd species identified by XPS likely originated from superficial oxidation during the sample handling and preparation under

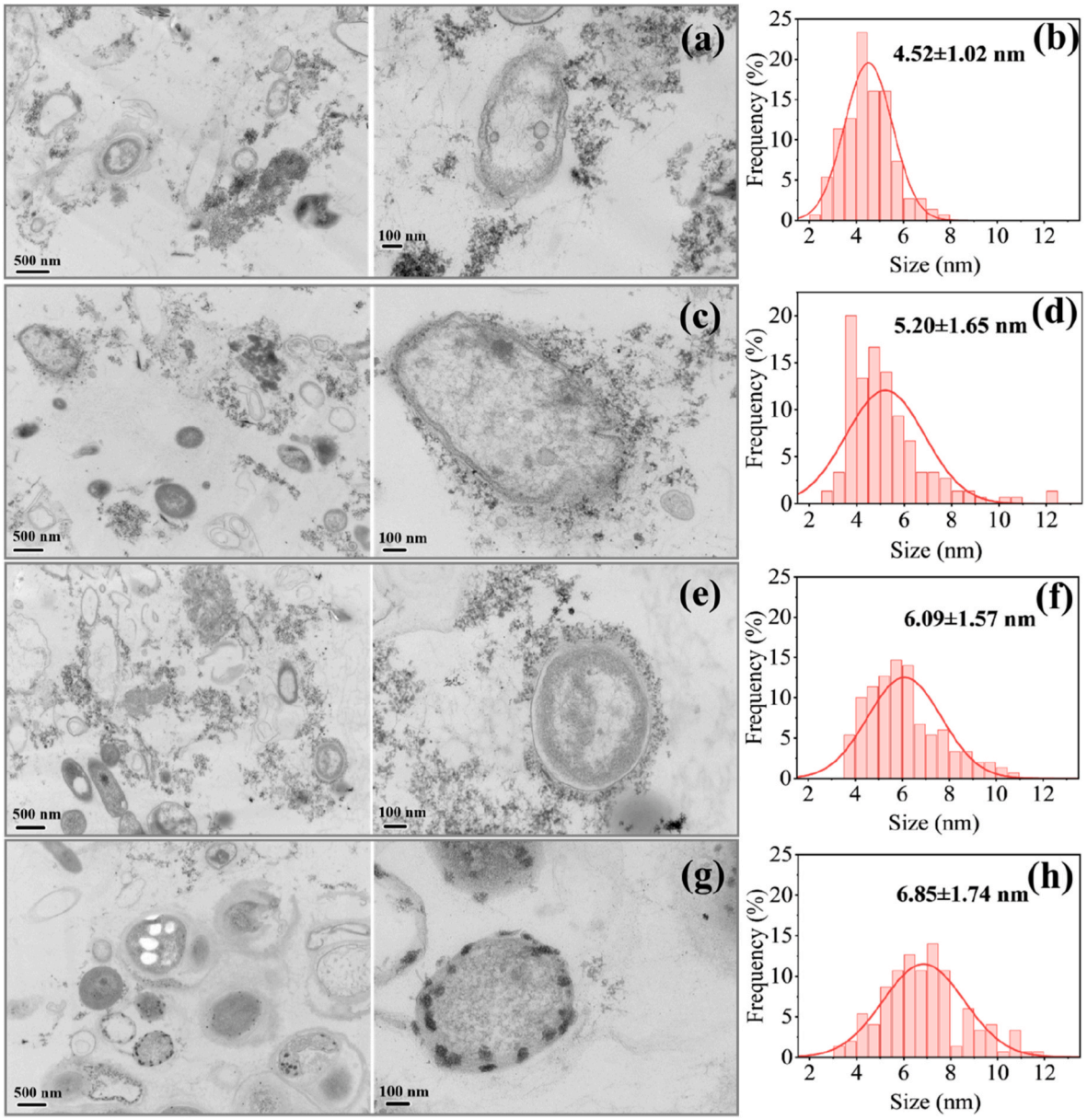

Fig. 2. Solid characterization of Pd^0@AAS with different Pd loadings: TEM images and Pd^0 particle size histograms for the four Pd loadings: 1.1 wt% (a, b); 2.7 wt% (c, d); 5.3 wt% (e, f); 10.6 wt% (g, h).

ambient conditions (Liu et al., 2022; Zhou et al., 2017). Notably, the characteristic diffraction patterns of PdO remain undetected in corresponding XRD profiles, corroborating the negligible concentration of such oxidized phases. Given the low proportion of Pd^{2+} in the catalyst, the influence of Pd^0/Pd^{2+} on the catalysis of DCF has not been considered in this study. This collective evidence conclusively verifies the predominant formation of Pd^0 nanoparticles within the AAS.

The TEM images (Fig. 2) show the morphology, distribution and size of the Pd^0 nanoparticles in AAS for four Pd loadings (1.1–10.6 wt%). The various Pd loadings explored in this research exerted negligible influence on the morphology and dispersion pattern of Pd^0 nanoparticles. Across all experimental conditions, Pd^0 manifested as discrete particles, predominantly residing within EPS, with a minor fraction located on the cell wall or in the periplasmic spaces. This distribution and morphological profile align closely with those reported in previous studies utilizing H_2 as an electron donor and anaerobic biofilm or activated sludge as a biocatalyst for Pd^0 production (Wu et al., 2022; Zhou et al., 2020). Since no Pd was detected in the effluent, it can be concluded that all Pd^0 was reduced and deposited within the AAS matrix.

TEM analysis reveals that Pd^0 nanoparticles are predominantly distributed within a narrow size range of 1–14 nm (Fig. 2(b), (d), (f), (h)), showing consistency with the dimensions reported for anaerobic granular sludge (AGS)-synthesized Pd^0 (Quan et al., 2019). The raw images and the complete dataset used for this size distribution analysis are provided in Fig. S2 and Table S2, respectively. A clear increasing trend in nanoparticle size was observed with rising Pd loading. Specifically, the mean particle diameter increased from 4.52 ± 1.02 nm at Pd loading 1.1 wt% to 6.85 ± 1.74 nm at Pd loading 10.6 wt% (Fig. S3). The corresponding polydispersity indices remained low (0.05–0.10), indicating relatively uniform populations at each condition. The smallest mean particle size of 4.52 ± 1.02 nm (PDI = 0.05) was achieved at the lowest Pd loading of 1.1 wt%, which is consistent with the typical size range (3–5 nm) reported for biofilm-synthesized Pd^0 nanoparticles (Long et al., 2021; Wu et al., 2022, 2024).

This phenomenon can be mechanistically explained through two competing pathways governing nanoparticle formation: the primary mechanism involves the dual reduction processes of Pd^{2+} precursors. During biosynthesis of Pd^0 nanoparticles using H_2 or formate as electron donors, the reduction of Pd^{2+} occurs through both enzymatic and autocatalytic pathways (Li et al., 2024). The latter becomes increasingly dominant at higher Pd loadings, where initially formed Pd^0 nanoparticles catalyze the further reduction of additional Pd^{2+} ions, leading to particle aggregation and growth (Zhou et al., 2016). This autocatalytic amplification effect results in progressively larger nanoparticles with increasing Pd concentration (Luo et al., 2022). Aggregates of Pd^0 nanoparticles were identified specifically at the highest Pd loading (10.6 wt%). These aggregates ranged from 17.7 to 87.9 nm in size, with an average diameter of 46.6 nm (Fig. S4). Due to their low abundance and indeterminate compactness, no further extensive discussion is warranted within the scope of this work, which centers on the properties of the dominant, well-dispersed nanoparticles.

Conversely, at lower Pd loadings, the system exhibits different growth dynamics due to the elevated biomass-to-Pd^{2+} ratio. The elevated biomass-to-Pd^{2+} ratio significantly enhances the enzymatic reduction pathway, which is known to produce smaller nanoparticles compared to autocatalytic reduction (Wu et al., 2022), while concurrently increasing the availability of biomolecular capping agents such as peptides. These microbial-derived peptides selectively bind to nanoparticle surfaces, effectively restricting particle growth and resulting in smaller, more uniform Pd^0 crystallites (Egan-Morriss et al., 2022). The combination of enhanced enzymatic reduction and surface capping accounts for the observed size reduction at lower Pd loadings.

3.2. The degradation pathway and ecotoxicity estimates

The transformation products (TPs) generated during DCF degradation were systematically identified through UPLC-MS analysis. Fig. 3(a) illustrates the temporal evolution of normalized chromatographic peak areas, demonstrating quantitative changes in the reaction composition throughout the catalytic process. Based on these observations and MS analysis, a degradation pathway is proposed in Fig. 3(b). The catalytic degradation initiates with Pd^0@AAS mediated hydrodechlorination. DCF first undergoes stepwise dechlorination, producing the intermediate 2-(2-((2-chlorophenyl)amino)phenyl)acetic acid (TP1, Cl-APA, *m/z* 261.06), followed by complete dechlorination to yield 2-anilinophenylacetic acid (TP2, APA, *m/z* 227.09). Alternatively, direct double dechlorination may occur to generate TP2. Subsequent hydrogenation preferentially targets the phenyl ring distal to the acetate group, forming 2-(2-(cyclohexylamino)phenyl)acetic acid (TP3, CPA, *m/z* 233.14) (Nieto-Sandoval et al., 2018). This regioselectivity arises from the fact that the steric hindrance and electron-withdrawing effect of the acetate group retard the hydrogenation of the connected phenyl ring. The complete hydrogenation of TP3 generates 2-[2-(cyclohexylamino)cyclohexyl]acetic acid (TP4, CCA, *m/z* 239.19), leading in full loss of aromaticity. An alternative pathway involves cyclohexyl elimination from TP3 to form 2-aminophenylacetic acid (TP5, AmPA, *m/z* 151.06). TP5 can then undergo further Pd^0-catalyzed hydrogenation to form 2-(2-aminocyclohexyl)acetic acid (TP6, AmCA, *m/z* 157.11), a compound readily metabolized by microorganisms.

The ecotoxicity of DCF and its identified TPs was predicted via the ECOSAR model (Ecological Structure-Activity Relationship) per the classification criteria listed in Table S4. For acute and chronic toxicity assessment, representative aquatic organisms (fish, daphnid, green algae) across trophic levels were selected (Ma et al., 2021, 2022). The toxicological effects and environmental persistence of aryl chlorides are largely attributable to the chlorine atoms in their molecular structure (Ding et al., 2018). As presented in Fig. 4, a clear negative correlation was observed between the number of chlorine substituents in the TPs and their acute/chronic toxicity. Specifically, DCF, which contains two chlorine atoms, exhibited the highest toxicity, followed by its mono-chlorinated derivative Cl-APA; in contrast, the fully dechlorinated APA showed substantially reduced toxicological effects. This structure-activity relationship suggests that sequential dechlorination during environmental transformation significantly attenuates the compound's ecotoxicological potential. However, chronic toxicity assessments revealed that APA still poses significant ecological risks, as it demonstrates persistent toxic effects on fish, daphnia, and green algae, with chronic toxicity thresholds (NOEC) 1-2 orders of magnitude lower than those of the parent compound DCF. Thus, further degradation of APA could enhance long-term environmental sustainability. CPA, the partially hydrosaturated derivative of APA, possesses comparable ecotoxicity to Cl-APA. However, upon subsequent elimination of the cyclohexyl group and complete hydrogenation, it can be further transformed into CCA, AmPA, and AmCA, which show no harm to aquatic organisms in terms of both acute and chronic toxicity.

Compared to the parent compound DCF, all TPs generated via Pd^0@AAS-catalyzed treatment exhibited reduced ecological toxicity. While complete dechlorination eliminated acute toxicity, hydrogenation and subsequent degradation processes eradicated chronic toxicity. Specifically, CCA, AmPA, and AmCA showed no acute or chronic toxicity, APA caused no acute harm to any of the three represented aquatic lives, Cl-APA and CPA showed no harm to fish and green algae in terms of acute toxicity, whereas DCF was estimated to exhibit both chronic toxicity and acute harmful effects on these aquatic organisms. Unlike conventional advanced oxidation processes (AOPs) mediated by oxygen-derived radicals (e.g., $\cdot SO_4^-$, ·OH, and $^1O_2$), which carry a higher risk of generating intermediates with elevated ecotoxicity compared to the parent contaminant(Fergani et al., 2025; Gackowska et al., 2025; Luo et al., 2025), the Pd^0@AAS system generated TPs with significantly reduced toxicity profiles. This result highlights the superior potential of the Pd^0@AAS system in terms of environmental safety.

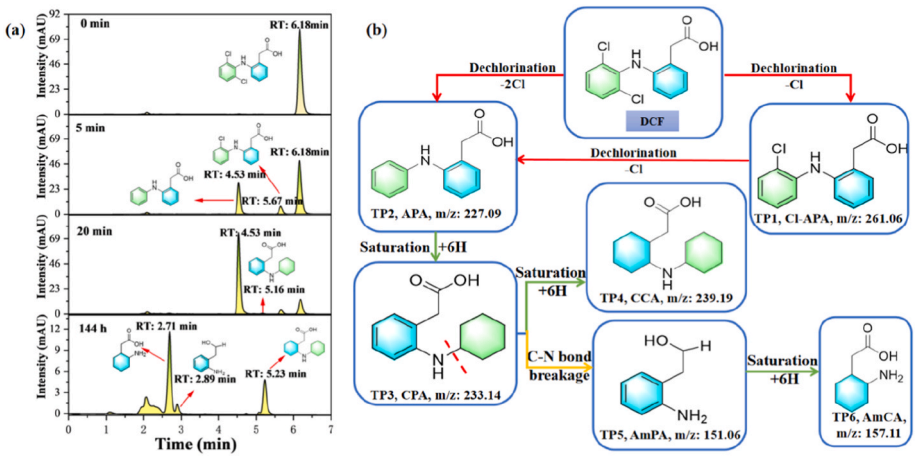

Fig. 3. The degradation pathway of Pd^0@AAS catalyzed DCF: HPLC chromatogram of Pd^0@AAS catalyzed DCF at H_2 atmosphere (Pd loading 2.7 wt%, pH = 7) (a) and Proposed reaction pathway for the catalytic degradation of DCF with H_2 over Pd^0@AAS (b).(Note: The peaks at 1 min and 2 min in the chromatogram originate from organic constituents inherently present in the AAS matrix).

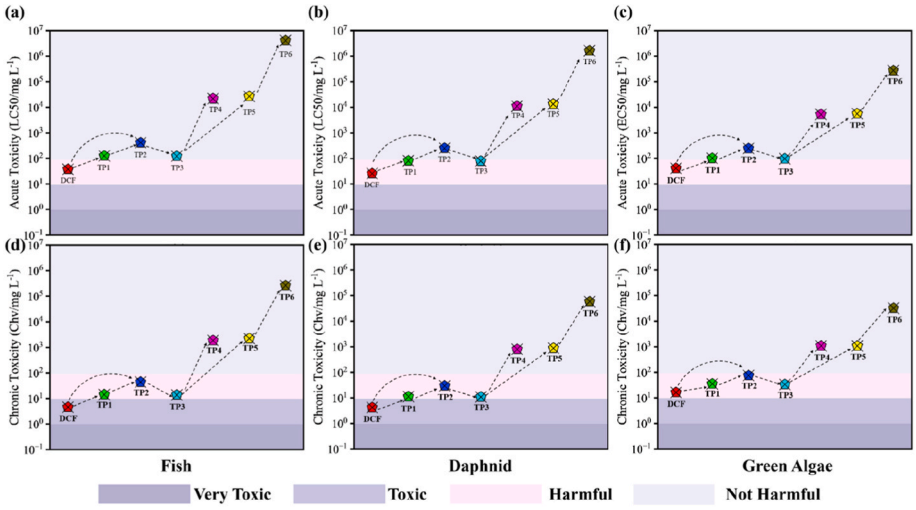

Fig. 4. Toxicity profiles of DCF and its transformation products (TPs) predicted via the ECOSAR model. Acute toxicity: Quantified by median lethal concentration (LC_{50}) and median effective concentration (EC_{50}), representing the concentrations required to induce 50 % mortality or sublethal effects in test organisms, respectively (a, b, c) and Chronic toxicity: Evaluated through chronic value (ChV), defined as the geometric mean of no-observed-effect concentration (NOEC) and lowest-observed-effect concentration (LOEC) for long-term ecological impacts (d, e, f).

3.3. The product selectivity of Pd^0@AAS catalyzed DCF

The Pd loading critically governs the product selectivity in Pd^0@AAS-catalyzed DCF degradation. The temporal evolution of DCF and its degradation products under varying Pd loadings is presented in Fig. 5. With Pd loading 1.1 wt% (Fig. 5 (a)), over 91.6 % DCF was dechlorinated to APA and Cl-APA within 250 min. No CPA was detected throughout the 250-min test, indicating that DCF was removed almost exclusively by hydrodechlorination, and the product stayed in APA. Only a small amount of APA was removed even after a few days of reaction (only about 17 % degradation was observed after 2.8 days). At Pd loadings 2.7, 5.3 and 10.6 wt% (Fig. 5(b)–(d)), over 99 % of DCF was depleted within 60 min, 10 min and <5 min, respectively, and the resulting APA undergoes efficient aromatic ring hydrogenation, with APA removal efficiencies ranging from 43 % to 100 %. During the reaction, no chlorinated CPA was detected, suggesting that hydrogenation of the DCF molecule did not precede hydrodechlorination.

Fig. 6 shows the proportion of different products during the catalytic reaction at 20 and 240 min. The DCF conversion exhibited strong Pd loading dependence at 20 min: 34.4 % at 1.1 wt%, 81.3 % at 2.7 wt%, and >99 % threshold achievement at 5.3 and 10.6 wt% Pd loadings (99.2 % and 100 %, respectively). The treatment efficiency achieved here compares favorably with that of other Pd-based catalysts for DCF degradation, as summarized in Table S5. The selectivity for Cl-APA decreases with increasing Pd loading, whereas the selectivity for APA exhibited an opposite trend (Fig. 6(a)). This indicates that low Pd loading tends to sequentially dechlorinate to obtain APA (first producing Cl-APA, which produces APA after dechlorination). In contrast, high Pd loading tends to directly generate APA through dechlorination in one step, especially when the Pd loading is 5.3 wt% and 10.6 wt%, the accumulation of Cl-APA is almost undetectable.

By 240 min, almost complete conversion of DCF (91.6–100 %) was achieved in all the Pd loadings. It is critical to note that, across all Pd loadings, detectable APA degradation was observed only after DCF was almost completely transformed—unequivocally demonstrating that Pd-catalyzed hydrodechlorination takes overwhelming priority over aromatic ring hydrogenation. The selectivity for APA decreased with the increase of Pd loading (Fig. 6(b)). At Pd loading 1.1 wt%, the system exhibited 89.7 % selectivity toward APA preservation. Conversely, at elevated Pd loading (10.6 wt%), complete hydrogenation of APA

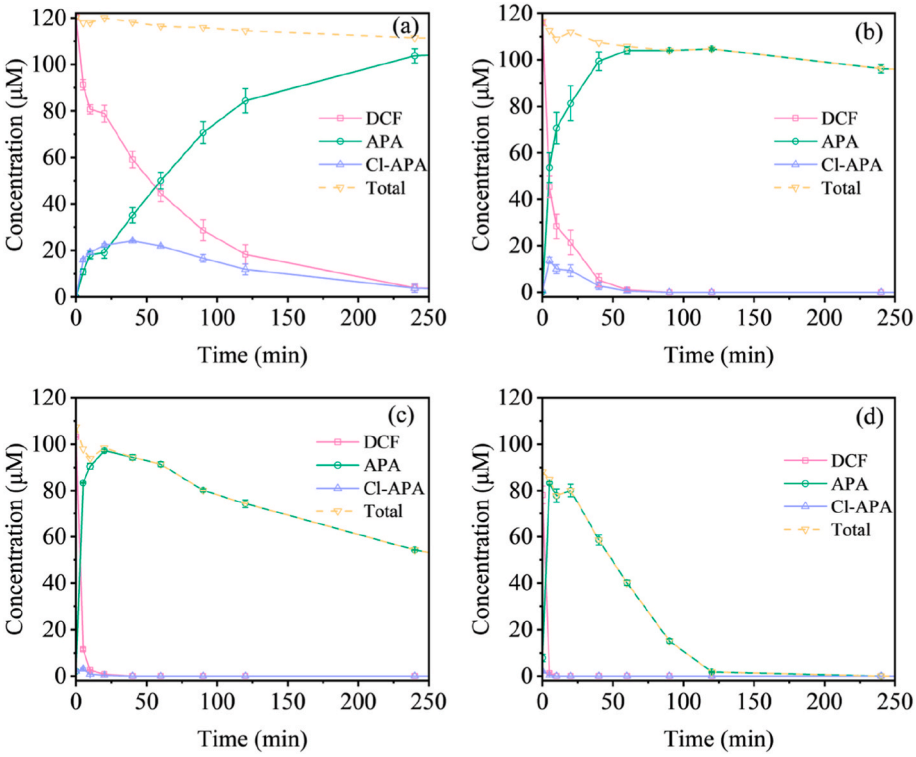

Fig. 5. Temporal evolution of DCF and its degradation products under varying Pd loadings: 1.1 wt% (a); 2.7 wt% (b); 5.3 wt% (c); 10.6 wt% (d).

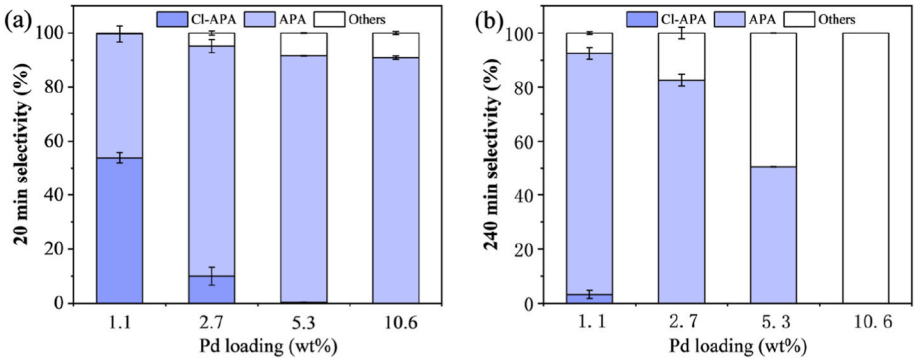

Fig. 6. Product selectivity of Pd^0@AAS catalyzed degradation of DCF for different Pd loadings: reaction time 20 min (a) and reaction time 240 min (b).

occurred with 0 % selectivity for it. This indicates that increasing the Pd loading helps to catalyze the hydrogenation of APA and transform it into nontoxic and more easily degradable compounds.

The observed difference in product selectivity is predominantly attributed to the availability of active sites on the catalysts, rather than their properties. For Pd^0-catalyzed degradation of chlorinated aromatic compounds, hydrodechlorination requires fewer Pd^0 active sites and H* (at least two active sites and one H* for the removal of one Cl atom). In contrast, hydrogenation can only be achieved when sufficient active sites are available (at least five active sites and three H* to saturate one benzene ring) (Luo et al., 2022). The catalytic system under low Pd loading conditions manifests dual constraints: (i) intrinsically limited abundance of Pd^0 nanoparticles, and (ii) exacerbated active-site occlusion by biomass-derived capping agents, which collectively suppress arene hydrogenation pathways requiring contiguous active sites. Baeza et al. (2016) reported analogous findings in experiments where polyvinylpyrrolidone (PVP)-capped Pd^0 catalysts were synthesized for the degradation of 4-CP. Specifically, phenol selectivity increased with higher PVP dosages, whereas cyclohexanone selectivity rose when PVP concentrations were reduced due to hydrogenation of phenol under these conditions. The moderate Pd^0 size variation (4.52 ± 1.02 to 6.85 ± 1.74 nm) in our system exerts a secondary influence on selectivity. Previous studies have proved that the hydrogenation of conjugated carbons in the benzene ring and carbon atoms in the C-Cl bond exhibits non-selectivity for nanoscale Pd-based catalysts (Brieger and Nestrick, 1974; Johnstone et al., 1985). This contrasts sharply with ligand-free synthesis systems, wherein sub-nanometric Pd clusters (0.33 ± 0.18 nm) generated at ultra-low loadings (0.02 g-Pd/m^2) completely suppressed aromatic ring hydrogenation, achieving >98 % phenolic selectivity. This high selectivity is attributed to the single-site nature of atomically dispersed Pd catalysts, which can be synthesized at low loadings to precisely control active site geometry and thus govern product distribution (Luo et al., 2022). It is worth noting that the superior selectivity towards dechlorination-only products of single Pd atom catalysts is commonly accompanied by catalytic activity decay and slow reaction kinetics (Chu et al., 2021); moreover, the resulting products are less favorable for pollutant treatment.

Catalyst reuse alters the selectivity toward DCF degradation

products. Fig. S5 illustrates the differences in catalytic performance between freshly prepared and reused Pd^0@AAS. Catalysts with low Pd loadings (1.1 and 2.7 wt%) nearly lost their activity. The main final product at a Pd loading of 5.3 wt% was APA. Only the highest Pd loading of 10.6 wt% maintained strong hydrodechlorination and hydrogenation capabilities, enabling complete removal of APA. This deactivation may be attributed to the fact that the first catalytic experiment was conducted over an extended period (2.8 days) to better investigate product selectivity. During this prolonged operation, microbial cell death likely occurred, releasing sulfur and increasing the sulfur content on the catalyst surface from 1.1 % to 2.7 % (obtained from the sample with a Pd loading of 2.7 wt%), which could have contributed to the poisoning of Pd active sites. This issue could be mitigated in the future by transitioning to a continuous-flow biofilm system. This operational mode better sustains microbial activity, thereby reducing the risk of sulfur release from cell lysis.

3.4. The hydrodechlorination and hydrogenation efficiency

Quantitative analysis reveals that the dependency of catalytic performance on Pd loading exhibits distinct profiles for DCF hydrodechlorination versus APA hydrogenation, although both reactions were well-fitted by pseudo-first-order kinetics. The kinetic constants and the values of these constants normalized to Pd concentration (i.e. catalyst-specific activity) are detailed in Table 1. The kinetic data reveal a striking 37- to 504-fold difference in first-order rate constants between DCF dechlorination and APA hydrogenation pathways, demonstrating significant differences in their activation barriers.

For hydrodechlorination (Fig. 7(a)), the reaction rate exhibited Pd loading dependence, with near-linear increases in rate constants as Pd loading rose from 1.1 wt% to 10.6 wt%. Consequently, increased Pd loading enhances hydrodechlorination efficiency. This trend is further supported by the time required to achieve chlorine balance (>95 %), which decreased significantly with increasing Pd loading: 450 min at 1.1 wt%, 60 min at 2.7 wt%, 20 min at 5.3 wt%, and only 5 min at 10.6 wt%. This contrasts with the findings of (Zhao et al., 2025) regarding the biogenic Pd-mediated degradation of 1,3,5-trinitro-1,3,5-triazinane (RDX). In their study, Pd loading exhibited an inverse correlation with RDX removal rate. This discrepancy arises because conductive Pd^0 nanoparticles primarily enhance RDX biodegradation by binding to cell membranes to facilitate bacterial extracellular electron transfer, whereas the direct chemical catalysis of RDX degradation by Pd plays a minimal role. In contrast, the removal of DCF relies predominantly on the chemical catalysis of Pd^0 nanoparticles, as microorganisms exhibit negligible capacity for DCF degradation (Fig. S6). Catalyst-specific activity, which was normalized by catalyst concentration, showed a near-linear increase when Pd loading ranged from 1.1 wt% to 5.3 wt%, followed by a pronounced plateau when Pd loading was between 5.3 wt % and 10.6 wt%. The highest Pd loading (10.6 wt%) only achieved a 16 % higher catalyst-specific activity than that of 5.3 wt%, and it was only 1.2-fold higher than 2.7 wt%. The occurrence of such a profile can be attributed to the following reason: within the lower Pd loading range (1.1–5.3 wt%), increasing Pd loading promoted the extracellular distribution of the Pd^0 nanoparticles, which offers more active sites for H_2 dissociative adsorption and enables direct contact with hydrophobic target molecules (Hou et al., 2017). At Pd loadings exceeding 5.3 wt%, where the active site density of Pd^0 nanoparticles no longer limited dechlorination kinetics, additional Pd loading-induced enhanced nanoparticles aggregation hindered the further improvement in catalyst-specific activity (Luo et al., 2022). This transition suggests the achievement of optimal Pd loading for DCF hydrodechlorination around 5.3 wt%, beyond which additional Pd loading yields minimal activity enhancement.

In contrast, both the rate constant and the catalyst-specific activity of hydrogenation maintain a strong, continuous dependence on Pd loading throughout the tested Pd loading range (Fig. 7(b)). The highest Pd loading (10.6 wt%) achieved a 2.7-fold higher catalyst-specific activity than that of 5.3 wt%, and it was almost 30-fold that of 2.7 wt%. The persistent sensitivity to Pd loading indicates that the hydrogenation pathway imposes higher demands on the number of active sites of the catalyst than the dechlorination pathway. This fundamental difference in Pd-loading dependence between the two reactions manifests clearly in Fig. 7(c), where the hydrogenation-to-dechlorination activity ratio exhibits a progressive increase with higher Pd loadings.

3.5. Pd catalyst poisoning and the potential restoration strategy

Catalyst poisoning is a major challenge for the practical, large-scale application of Pd catalysts. Sulfide, sulfate, SO_x and organosulfur species can react with Pd to form stable Pd sulfates and PdS, causing strong, often irreversible deactivation by blocking surface ensembles needed for hydrogenation/reduction. Natural/dissolved organic matter (NOM/DOM) and sulfur species adsorb strongly on metallic Pd nanoparticles at hollow sites, competitively occupying active sites and inhibiting reaction of target contaminants. Other water matrix components are recognized as foulants that cause long-term loss of activity and stability

Table 1
Kinetic results for DCF hydrochlorination and APA hydrogenation.

	DCF hydrodechlorination			APA hydrogenation		
Pd loading wt%	Rate constant (k_1) min^{-1}	R^2	Activity (k_{Pd1}) $L{\cdot}mmol^{-1}$-Pd$\cdot$ min^{-1}	Rate constant (k_2) min^{-1}	R^2	Activity (k_{Pd2}) $L{\cdot}mmol^{-1}$-Pd$\cdot$ min^{-1}
1.1	0.01287 ± 0.00111	0.96	0.06435 ± 0.00555	N.A.	N.A.	N.A.
2.7	0.10085 ± 0.01742	0.91	0.2017 ± 0.03484	0.00020 ± 0.00002	0.97	0.0004 ± 0.00004
5.3	0.37552 ± 0.05183	0.96	0.37552 ± 0.05183	0.00316 ± 0.00031	0.98	0.00316 ± 0.00031
10.6	0.86946 ± 0.00095	0.99	0.43473 ± 0.00048	0.02348 ± 0.00441	0.90	0.01174 ± 0.00221

"N.A." stands for not applicable.

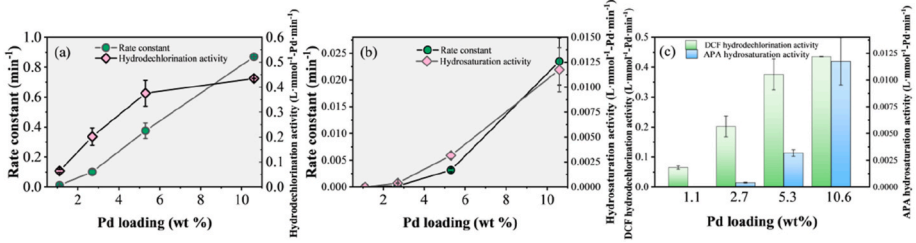

Fig. 7. DCF hydrodechlorination and APA hydrogenation kinetic parameter for different Pd loadings.

in Pd-based water treatment, primarily via competitive adsorption and pore/surface fouling. Inevitably, biosynthesized Pd catalysts are also susceptible to catalyst poisoning, as with other types of Pd catalysts. However, the adsorption of contaminant species by the inherent microbes and EPS can mitigate Pd poisoning. Furthermore, process design (such as pre-removal of strong foulants, staging of treatment steps, managing H_2 and co-contaminants) is emphasized as equally important as catalyst formulation for minimizing fouling and maintaining activity under realistic water matrices.

4. Conclusion

This study establishes Pd^0@AAS as a tunable catalytic system for the remediation of DCF, with Pd loading dictating degradation products and ecological outcomes. The main conclusions are: Pd^0@AAS selectively catalyzes hydrodechlorination at low Pd loadings (1.1 wt%), efficiently removing chlorine while retaining the aromatic structure. Higher Pd loadings (2.7–10.6 wt%) enable complete hydrogenation of the aromatic ring, forming less toxic aliphatic products and eliminating chronic ecological risks. Kinetic profiles reveal that dechlorination is optimal at moderate Pd loadings (5.3 wt%), whereas aromatic ring hydrogenation requires greater Pd availability due to its dependence on contiguous active sites. The system provides operational flexibility: lower Pd loadings offer cost-effective dechlorination, while higher Pd loadings ensure full detoxification. The biomass-supported catalyst combines environmental sustainability with tunable reactivity, offering a promising solution for halogenated aromatic pollutant remediation that can be adapted to specific treatment objectives and regulatory requirements.

CRediT authorship contribution statement

Xiaodi Li: Writing – original draft, Investigation, Data curation. **Jingzhou Zhou:** Writing – review & editing, Data curation. **Lin Yang:** Writing – review & editing, Methodology. **Si Pang:** Writing – review & editing, Formal analysis. **Yi Yang:** Writing – review & editing. **Defu Gan:** Visualization. **Junxia He:** Writing – review & editing. **Penghui Shi:** Writing – review & editing. **Siqing Xia:** Writing – review & editing, Supervision, Funding acquisition.

Declaration of competing interest

The authors declare that they have no known competing financial interests or personal relationships that could have appeared to influence the work reported in this paper.

Acknowledgments

The work was supported by the National Key Project of Research and Development Plan of China (Grant No. 2021YFC3201300).

Appendix A. Supplementary data

Supplementary data to this article can be found online at https://doi.org/10.1016/j.jclepro.2026.147676.

Data availability

Data will be made available on request.

References

Baeza, J.A., Calvo, L., Rodriguez, J.J., Gilarranz, M.A., 2016. Catalysts based on large size-controlled Pd nanoparticles for aqueous-phase hydrodechlorination. Chem. Eng. J. 294, 40–48. https://doi.org/10.1016/j.cej.2016.02.107.

Barreto Torres, L.D., dos Santos, M., Silva Queiróz, S., Gomes Coelho, L.H., 2022. Assessment of diclofenac adsorption into activated sludge: mechanism and thermodynamic. J. Env. Eng. Crit. Chall. 1 (1), 101. https://doi.org/10.33790/jeecc1100101.

Bartrons, M., Peñuelas, J., 2017. Pharmaceuticals and personal-care products in plants. Trends Plant Sci. 22 (3), 194–203. https://doi.org/10.1016/j.tplants.2016.12.010.

Brieger, G., Nestrick, T.J., 1974. Catalytic transfer hydrogenation. Chem. Rev. 74 (5), 567–580. https://doi.org/10.1021/cr60291a003.

Chhaya, Raychoudhury, T., Bag, R., 2025. Insight into the diclofenac and carbamazepine removal by *Bacillus subtilis* BMT4i immobilized on different activated carbons: a comparative removal study by activated carbon, bacterial cell, and its composite. Int. J. Environ. Res. 19 (1), 28. https://doi.org/10.1007/s41742-024-00687-2.

Chu, C., Huang, D., Gupta, S., Weon, S., Niu, J., Stavitski, E., Muhich, C., Kim, J.-H., 2021. Neighboring Pd single atoms surpass isolated single atoms for selective hydrodehalogenation catalysis. Nat. Commun. 12 (1), 5179. https://doi.org/10.1038/s41467-021-25526-2.

Dalahmeh, S., Bjornberg, E., Elenstrom, A.-K., Niwagaba, C.B., Komakech, A.J., 2020. Pharmaceutical pollution of water resources in Nakivubo wetlands and Lake Victoria, Kampala, Uganda. Sci. Total Environ. 710, 136347. https://doi.org/10.1016/j.scitotenv.2019.136347.

De Corte, S., Hennebel, T., Fitts, J.P., Sabbe, T., Bliznuk, V., Verschuere, S., van der Lelie, D., Verstraete, W., Boon, N., 2011. Biosupported bimetallic Pd–Au nanocatalysts for dechlorination of environmental contaminants. Environ. Sci. Technol. 45 (19), 8506–8513. https://doi.org/10.1021/es2019324.

De Corte, S., Sabbe, T., Hennebel, T., Vanhaecke, L., De Gusseme, B., Verstraete, W., Boon, N., 2012. Doping of biogenic Pd catalysts with Au enables dechlorination of diclofenac at environmental conditions. Water Res. 46 (8), 2718–2726. https://doi.org/10.1016/j.watres.2012.02.036.

Ding, X., Yao, Z., Xu, Y., Liu, B., Liu, Q., She, Y., 2018. Aqueous-phase hydrodechlorination of 4-chlorophenol on palladium nanocrystals: identifying the catalytic sites and unraveling the reaction mechanism. J. Catal. 368, 336–344. https://doi.org/10.1016/j.jcat.2018.10.008.

Egan-Morriss, C., Kimber, R.L., Powell, N.A., Lloyd, J.R., 2022. Biotechnological synthesis of Pd-based nanoparticle catalysts. Nanoscale Adv. 4 (3), 654–679. https://doi.org/10.1039/d1na00686j.

Fergani, S., Zazoua, H., Saadi, A., Badri, F.Z., Boudjemaa, A., Bachari, K., 2025. Catalytic degradation of diclofenac by ZnO-Co_3O_4: identification of major intermediates and degradation pathway. Environ. Sci. Pollut. Res. 32 (4), 1971–1984. https://doi.org/10.1007/s11356-024-35713-5.

Fontes, M.K., Gusso-Choueri, P.K., Maranho, L.A., Abessa, D.M.d.S., Mazur, W.A., de Campos, B.G., Guimarães, L.L., de Toledo, M.S., Lebre, D., Marques, J.R., Felicio, A. A., Cesar, A., Almeida, E.A., Pereira, C.D.S., 2018. A tiered approach to assess effects of diclofenac on the brown mussel Perna perna: a contribution to characterize the hazard. Water Res. 132, 361–370. https://doi.org/10.1016/j.watres.2017.12.077.

Gackowska, A., Studziński, W., Kudlek, E., Przybyłek, M., 2025. Environmental fate and ecotoxicity of diclofenac degradation products generated by photo-assisted advanced oxidation processes. J. Hazard. Mater. 489, 137708. https://doi.org/10.1016/j.jhazmat.2025.137708.

González García, M., Fernández-López, C., Pedrero-Salcedo, F., Alarcón, J.J., 2018. Absorption of carbamazepine and diclofenac in hydroponically cultivated lettuces and human health risk assessment. Agric. Water Manag. 206, 42–47. https://doi.org/10.1016/j.agwat.2018.04.018.

He, H., Li, Y., Shen, R., Shim, H., Zeng, Y., Zhao, S., Lu, Q., Mai, B., Wang, S., 2021. Environmental occurrence and remediation of emerging organohalides: a review. Environ. Pollut. 290, 118060. https://doi.org/10.1016/j.envpol.2021.118060.

Hou, Y.-N., Zhang, B., Yun, H., Yang, Z.-N., Han, J.-L., Zhou, J., Wang, A.-J., Cheng, H.-Y., 2017. Palladized cells as suspension catalyst and electrochemical catalyst for reductively degrading aromatics contaminants: roles of Pd size and distribution. Water Res. 125, 288–297. https://doi.org/10.1016/j.watres.2017.08.055.

Johnstone, R.A.W., Wilby, A.H., Entwistle, I.D., 1985. Heterogeneous catalytic transfer hydrogenation and its relation to other methods for reduction of organic compounds. Chem. Rev. 85 (2), 129–170. https://doi.org/10.1021/cr00066a003.

Kwidzińska, K., Zalewska, M., Aksmann, A., Kobos, J., Mazur-Marzec, H., Caban, M., 2024. Multi-biomarker response of Cyanobacteria *Synechocystis salina* and *Microcystis aeruginosa* to diclofenac. J. Hazard. Mater. 471, 134373. https://doi.org/10.1016/j.jhazmat.2024.134373.

Law, C.K.Y., Bonin, L., De Gusseme, B., Boon, N., Kundu, K., 2022. Biogenic synthesis of palladium nanoparticles: new production methods and applications. Nanotechnol. Rev. 11 (1), 3104–3124. https://doi.org/10.1515/ntrev-2022-0482.

Li, X., Yang, L., Zhou, J., Dai, B., Gan, D., Yang, Y., Wang, Z., He, J., Xia, S., 2024. Biogenic palladium nanoparticles for wastewater treatment: formation, applications, limitations, and future directions. J. Water Process Eng. 64, 105641. https://doi.org/10.1016/j.jwpe.2024.105641.

Li, X., Yang, Y., Wang, J., Jin, H., Zhang, Y., Cui, Y., Song, Y., Yan, J., 2022. Organohalide respiration with diclofenac by dehalogenimonas. Environ. Sci. Technol. 56 (16), 11266–11276. https://doi.org/10.1021/acs.est.1c08824.

Liu, Y., Xi, Y., Xie, T., Liu, H., Su, Z., Huang, Y., Xu, W., Wang, D., Zhang, C., Li, X., 2022. Enhanced removal of diclofenac via coupling Pd catalytic and microbial processes in a H_2-based membrane biofilm reactor: performance, mechanism and biofilm microbial ecology. Chemosphere 307 (1), 135597. https://doi.org/10.1016/j.chemosphere.2022.135597.

Long, M., Long, X., Zheng, C.-W., Luo, Y.-H., Zhou, C., Rittmann, B.E., 2021. Para-chlorophenol (4-CP) removal by a palladium-coated biofilm: coupling catalytic dechlorination and microbial mineralization via denitrification. Environ. Sci. Technol. 55 (9), 6309–6319. https://doi.org/10.1021/acs.est.0c08307.

Luo, D., Zhang, H., An, X., Zhao, J., Feng, C., Yin, J., Luo, M., Wei, T., Liu, Y., Shi, Y., Zhang, J., Lai, B., 2025. Synergistic effects of sulfur-doped carbon dots/

permanganate process for DCF degradation: mechanism and pathways. J. Hazard. Mater. 494, 138567. https://doi.org/10.1016/j.jhazmat.2025.138567.

Luo, Y.-H., Cai, Y., Long, X., Zhou, D., Zhou, C., Rittmann, B.E., 2022. Palladium (Pd^0) loading-controlled catalytic activity and selectivity for chlorophenol hydrodechlorination and hydrosaturation. Environ. Sci. Technol. 56 (7), 4447–4456. https://doi.org/10.1021/acs.est.1c08347.

Ma, D., Wang, J., Feng, K., Liu, B., Xie, G., Xing, D., 2022. A green strategy from waste red mud to Fe^0-based biochar for sulfadiazine treatment by peroxydisulfate activation. Chem. Eng. J. 446, 136944. https://doi.org/10.1016/j.cej.2022.136944.

Ma, D., Yang, Y., Liu, B., Xie, G., Chen, C., Ren, N., Xing, D., 2021. Zero-valent iron and biochar composite with high specific surface area via K_2FeO_4 fabrication enhances sulfadiazine removal by persulfate activation. Chem. Eng. J. 408, 127992. https://doi.org/10.1016/j.cej.2020.127992.

Nieto-Sandoval, J., Munoz, M., de Pedro, Z.M., Casas, J.A., 2018. Fast degradation of diclofenac by catalytic hydrodechlorination. Chemosphere 213, 141–148. https://doi.org/10.1016/j.chemosphere.2018.09.024.

Nieto-Sandoval, J., Sanchez, R., Munoz, M., de Pedro, Z.M., Casas, J.A., 2022. Catalytic hydrodehalogenation of the flame retardant tetrabromobisphenol A by alumina-supported Pd, Rh and Pt catalysts. Chem. Eng. J. Adv. 9, 100212. https://doi.org/10.1016/j.ceja.2021.100212.

Nosek, K., Zhao, D., 2024. Transformation products of diclofenac: formation, occurrence, and toxicity implication in the aquatic environment. Water Res. 266, 122388. https://doi.org/10.1016/j.watres.2024.122388.

Oaks, J.L., Gilbert, M., Virani, M.Z., Watson, R.T., Meteyer, C.U., Rideout, B.A., Shivaprasad, H.L., Ahmed, S., Iqbal Chaudhry, M.J., Arshad, M., Mahmood, S., Ali, A., Ahmed Khan, A., 2004. Diclofenac residues as the cause of vulture population decline in Pakistan. Nature 427 (6975), 630–633. https://doi.org/10.1038/nature02317.

Qiu, B., Zhou, X., Li, W., Zhu, H., Yu, L., Yuan, C., Dou, R., Sun, M., Wang, S., 2024. A magnetically induced self-assembly of Ru@Fe_3O_4/rGO cathode for diclofenac degradation in electro-Fenton process. Environ. Res. 242, 117781. https://doi.org/10.1016/j.envres.2023.117781.

Quan, X., Wang, X., Sun, Y., Li, W., Chen, L., Zhao, J., 2019. Degradation of diclofenac using palladized anaerobic granular sludge: effects of electron donor, reaction medium and deactivation factors. J. Hazard. Mater. 365, 155–163. https://doi.org/10.1016/j.jhazmat.2018.10.100.

Sales, D.A., Jerônimo, A.G., Trigueiro, P., Albuquerque, W., Barbosa, R., Neves, L., Almeida, L.C., Guerra, Y., Osajima, J.A., Padrón-Hernández, E., Viana, B.C., Peña-Garcia, R.R., 2025. Synergistic effects of Al^{3+}/La^{3+} co-doped ZnO photocatalysts for enhanced removal of remazol red dye and diclofenac in aqueous solutions. Colloids Surf. A Physicochem. Eng. Asp. 709, 136130. https://doi.org/10.1016/j.colsurfa.2025.136130.

Schmidt, S., Hoffmann, H., Garbe, L.-A., Schneider, R.J., 2018. Liquid chromatography-tandem mass spectrometry detection of diclofenac and related compounds in water samples. J. Chromatogr. A 1538, 112–116. https://doi.org/10.1016/j.chroma.2018.01.037.

Wu, C., Zhou, J., Pang, S., Yang, L., Li, X., Lichtfouse, E., Xia, S., Liu, H., 2024. Enhanced removal of 2,4-dichlorophenol by coupling of Pd nanoparticles with biofilm. J. Environ. Chem. Eng. 12 (2), 112176. https://doi.org/10.1016/j.jece.2024.112176.

Wu, C., Zhou, L., Zhou, C., Zhou, Y., Zhou, J., Xia, S., Rittmann, B.E., 2022. A kinetic model for 2,4-dichlorophenol adsorption and hydrodechlorination over a palladized biofilm. Water Res. 214, 118201. https://doi.org/10.1016/j.watres.2022.118201.

Xu, D., Du, B., Jiang, X., Ling, J., Xiao, S., Sun, H., Yin, X., 2025. Sorption behavior of diclofenac sodium and venlafaxine on microplastics: a mechanistic study based on spectroscopy and density functional theory. J. Clean. Prod. 518, 145960. https://doi.org/10.1016/j.jclepro.2025.145930.

Zhang, Y., Geißen, S.-U., Gal, C., 2008. Carbamazepine and diclofenac: removal in wastewater treatment plants and occurrence in water bodies. Chemosphere 73 (8), 1151–1161. https://doi.org/10.1016/j.chemosphere.2008.07.086.

Zhao, S., Hou, B., Zhang, K., Jia, Y., Lu, J., 2025. Biogenic palladium nanoparticles reclaimed by a novel strain *Citrobacter braakii* Z1 accelerating RDX biodegradation in the munition effluent. Int. Biodeterior. Biodegrad. 201, 106075. https://doi.org/10.1016/j.ibiod.2025.106075.

Zhao, W., Duan, Z., Zheng, Z., Li, B., 2022. Cobalt bismuth oxide with cobalt(II/III) as a new stable peroxymonosulfate activator for effective degradation, mineralization, and detoxification of diclofenac in water. J. Clean. Prod. 365, 132781. https://doi.org/10.1016/j.jclepro.2022.132781.

Zhou, C., Ontiveros-Valencia, A., Wang, Z., Maldonado, J., Zhao, H.-P., Krajmalnik-Brown, R., Rittmann, B.E., 2016. Palladium recovery in a H_2-based membrane biofilm reactor: formation of Pd(0) nanoparticles through enzymatic and autocatalytic reductions. Environ. Sci. Technol. 50 (5), 2546–2555. https://doi.org/10.1021/acs.est.5b05318.

Zhou, C., Wang, Z., Ontiveros-Valencia, A., Long, M., Lai, C.-y., Zhao, H.-p., Xia, S., Rittmann, B.E., 2017. Coupling of Pd nanoparticles and denitrifying biofilm promotes H_2-based nitrate removal with greater selectivity towards N_2. Appl. Catal. B Environ. 206, 461–470. https://doi.org/10.1016/j.apcatb.2017.01.068.

Zhou, L., Wu, C., Xie, Y., Xia, S., 2020. Biogenic palladium prepared by activated sludge microbes for the hexavalent chromium catalytic reduction: impact of relative biomass. Front. Environ. Sci. Eng. 14 (2), 27. https://doi.org/10.1007/s11783-019-1206-4.